

MESOM: A MOON-ENABLED SUN OCCULTATION MISSION

Nicola Baresi, Lucie Green, Huw Morgan, Craig Underwood, Chris Bridges, Andrea Lucca Fabris, Keith Ryden, Steve Eckersley

The study of the solar corona has important ramifications on the understanding and forecasting of coronal mass ejections, solar flares, and solar energetic particle events that can pose a significant threat to society. Yet, regardless of scientific breakthroughs brought by space-based coronagraphs, access to the lowest layers of the Sun's atmosphere remains challenging because of vignetting and stray light effects that significantly degrade signal-to-noise ratios in these regions. An alternative approach, first proposed by Eckersley and Kemble, advocates creating artificial total eclipses in space by flying a spacecraft in the shadow of the Moon. This paper introduces the preliminary trajectory design analyses and trade-off studies of a Moon-Enabled Sun Occultation Mission (MESOM). By means of synodic resonant orbits that exists in the chaotic dynamics of the Sun-Earth-Moon system, trajectories capable of delivering on average 15 minutes per synodic month (29.6 days circa) of manoeuvre-free solar corona observations below 1.02 sun radii were identified and used as a baseline for the preliminary design of a 2+ year-long satellite mission.

keywords: MESOM, Space Mission Design, Solar Corona, Space Weather.

1. INTRODUCTION

Solar flares, Solar Energetic Particle Events (SEPE) and coronal mass ejections (CME) are common space weather events that can sometimes be so powerful to cause disruption to technological and communication systems on which modern society depends upon.¹ It is estimated that a geomagnetic storm caused by solar activity in March 1989 cost more than 6.5M USD in material damage following a 9-hour power blackout in Quebec.² The storm was triggered by a CME that was an order of magnitude less powerful than the one causing the more infamous 1859 Carrington event, in which sparks originating from telegraph machines were reported to shock operators and set papers ablaze.³ Nowadays, the consequences of a storm of these proportions would be even more catastrophic, as repeatedly recognized by world-wide governments, including the UK*. SEPEs can indeed be lethal for astronauts working in exposed locations such as the lunar surface.^{4,5}

Despite the consequences of solar activity on ground and space-based technologies, and the knock-on societal and economic impact, accurate forecasting of solar events remains elusive. This directly relates to the many open questions that currently exist in fundamental solar physics and to which answers are being sought. To achieve progress in both space weather forecasting and fundamental solar science re-

quires high-quality observations of the Sun's atmosphere (where space weather events originate) from the base of the atmosphere up to a distance of several solar radii. The only way currently to achieve such observations is to use a coronagraph that blocks the disc of the Sun and creates an artificial solar eclipse.⁶ However, vignetting and stray light effects hamper the ability to use a coronagraph to clearly image the lowest layers of the solar atmosphere.^{7,8} The best method remains taking images during a natural total solar eclipse during which time the Moon blocks the Sun. However, these are extremely rare events that typically last for a few minutes and only happens once every 18 months, on average.

In order to capitalise on the unique opportunities afforded when the Moon occults the Sun, Eckersley and Kemble proposed to fly a spacecraft in the shadow cast by a celestial object,⁹ thus enabling prolonged and high-quality measurements of the lower corona down to the Sun's chromosphere (Fig. 1). This concept is originally demonstrated using fuel-expensive spacecraft trajectories that are designed under the assumptions of the Earth-spacecraft two-body problem. Such a dynamical approximation is overly optimistic and neglects important contributions due to the gravitational attractions of the Sun and the Moon.¹⁰

This paper introduces the preliminary trajectory design analyses and trade-off studies of a Moon-Enabled Sun Occultation Mission (MESOM). Using

*<https://www.gov.uk/government/publications/national-risk-register-for-civil-emergencies-2012-update>

2. Calculating the Occultation Zone

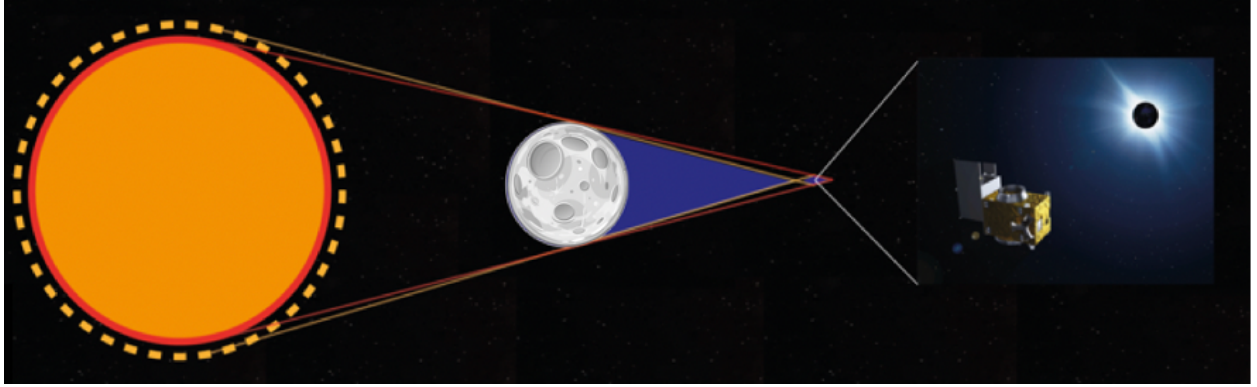


Fig. 1: Artistic view of the Eckersley-Kemble Sun occultation concept. Credit: N. Bernardini

the Moon as a natural occulter avoids the technical challenges of a coronagraph optical system and contributes to mitigate some of the design issues and pointing requirements of large-scale space-based coronagraphs as discussed by Habbal and others.^{11–13} MESOM does not require coronagraphic capabilities, and, given an appropriate orbit, can collect high-resolution high-quality data of the inner solar corona for a time equivalent to 35 total solar eclipses on Earth. These unprecedented measurements will fill a gap in current existing spaceborne capabilities and unlock a better understanding and forecasting of adverse space weather phenomena.

2. CALCULATING THE OCCULTATION ZONE

The Sun's occultation zone is hereby defined as the region in the Moon's umbra cone where the apparent size of the Moon directly occult the solar disk, thus enabling direct observations of the inner corona. The perimeter of the region is determined by drawing tangent lines from the Sun to the Moon, and by considering a larger fictitious Sun corresponding to the maximum tolerated distance from the Sun's photosphere (the red and yellow lines of Fig. 1). In this study, a fictitious Sun radii of $1.02 R_{\odot}$ is used for the Moon's occultation region such that direct observations of the inner corona, down to at least $1.02 R_{\odot}$ radii, can be guaranteed by passage through the occultation zone. A zoom-in of the Sun's occultation zone is offered in Fig. 2, whereby the four location P_1 , P_2 , P_{y+} and P_{y-} are introduced. These points delimit the area of the region of interest as follows. P_1 is located along the Sun-Moon direction at the intersection between this line and the tangent to the Moon's and Sun's nominal radii. A spacecraft located in P_1 would experience a total eclipse with magnitude 1.

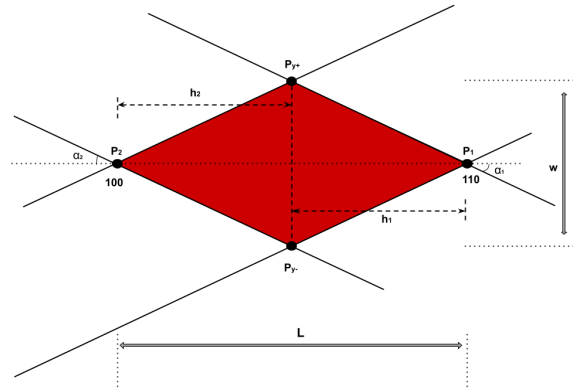


Fig. 2: Zoom-in of the Moon-enabled Sun occultation zone. Credit: D. Ladan-Baki.

Conversely, P_2 is located along the same Sun-Moon direction, but at a distance from the Moon whereby the total eclipse has a magnitude of 1.02. That is, the apparent size of the Moon would be 1.02 the apparent size of the Sun.

Using geometrical relationships and denoting l_1 as the distance between the P_1 point and the barycentre of the Moon, it is found that

$$R_{s1} = (d_{sm} + l_1) \sin(\alpha_1), \quad [1a]$$

$$R_m = l_1 \sin(\alpha_1), \quad [1b]$$

where d_{sm} denotes the instantaneous distance between the Sun and the Moon; $R_{s1} = R_{\odot} = 695\,550$ km is the nominal radius of the Sun; $R_m = 1737.1$ km is the nominal radius of the Moon; α_1 is the half-cone angle of the Moon's umbra cone. Solving Eq. [1] for

3. Trajectory Design

l_1 and α_1 yields

$$l_1 = \left(\frac{R_m}{R_{s_1} - R_m} \right) d_{sm}, \quad [2a]$$

$$\alpha_1 = \arcsin \left(\frac{R_m}{l_1} \right), \quad [2b]$$

whereas

$$l_2 = \left(\frac{R_m}{R_{s_2} - R_m} \right) d_{sm}, \quad [3a]$$

$$\alpha_2 = \arcsin \left(\frac{R_m}{l_2} \right), \quad [3b]$$

can be found from similar derivations in which $R_{s_2} = 1.02 R_\odot$. The length of the occultation zone becomes

$$L = l_1 - l_2 = R_m \left[\frac{R_{s_2} - R_{s_1}}{(R_{s_1} - R_m)(R_{s_2} - R_m)} \right] d_{sm}, \quad [4]$$

thereby illustrating how both the Sun-Moon distance and expansion factor contribute to the size of the occultation zone.

As far as the width of the occultation zone is concerned, let us observe that, in three-dimensional space, the zone would appear as a bicone aligned with the Sun-Moon direction. The two half-heights, h_1 and h_2 would satisfy

$$L = h_1 + h_2, \quad [5a]$$

$$w = 2 h_1 \tan(\alpha_1) = 2 h_2 \tan(\alpha_2), \quad [5b]$$

with w as the width of the Moon's occultation zone or maximum diameter of the three-dimensional bicone. By solving Eq. [5] for h_1 and h_2 , one finds that

$$h_1 = \frac{\tan(\alpha_2)}{\tan(\alpha_1) + \tan(\alpha_2)} L, \quad [6a]$$

$$h_2 = \frac{\tan(\alpha_1)}{\tan(\alpha_1) + \tan(\alpha_2)} L, \quad [6b]$$

$$w = 2 \left[\frac{\tan(\alpha_1) \tan(\alpha_2)}{\tan(\alpha_1) + \tan(\alpha_2)} \right] L, \quad [6c]$$

thereby illustrating how the width of the target zone may also vary with changes in the expansion factor and d_{sm} values through L .

Equations [4] and [6c] display where the main challenges associated with a Moon-enabled Sun occultation mission might be. Indeed, while the expansion factor is a constant user-defined parameter that can be adjusted depending on the navigation and scientific requirements of the mission, d_{sm} values are subject to changes due to the mutual gravitational interaction between the Sun, the Earth, and the Moon.

Figure 3 reveals how d_{sm} would vary over one year, starting from Apr 25 2023 at 12:00:00 (UTC). The values of d_{sm} are obtained via NASA's SPICE kernels, containing the most accurate estimation of the Sun and Moon's locations publicly available to space engineers.[†] Shown in the same figure are the L and w values recorded throughout this preliminary investigation. As can be seen, w remains fairly constant and close to the nominal value of 34.49 km. Conversely, L exhibits long-term oscillations between $L_{min} = 7200$ km and $L_{max} = 7500$ km caused by the non-Keplerian dynamics of the Sun-Earth-Moon system. To account for this time-varying dynamical environment, MESOM baseline trajectories are first calculated in the Sun-Earth-Moon Bi-Circular Problem (BCP) and later re-optimized under the real-world dynamics of the Sun-Earth-Moon-spacecraft four body problem while seeking for fuel-efficient trajectories that pass through the time-varying occultation zone introduced in this Section.

3. TRAJECTORY DESIGN

To collect high-quality measurements of the inner sun corona, MESOM will repeatedly pass near the apex of the Moon's umbra region while coping with the chaotic dynamics of the Sun-Earth-Moon system. It follows that Synodic Resonant Periodic Orbits (SRPO), i.e., periodic orbits in the Sun-Earth-Moon four-body problem whose period is multiple of the orbital period of the Sun around the Earth-Moon barycentre ($P_s = 29.6$ days), would appear to be natural candidate for minimizing fuel-consumption while guaranteeing that the spacecraft would return to the Sun occultation zone for new observations.^{14–17}

To begin with, let us consider the case in which the spacecraft, the Sun, the Earth, and the Moon are all co-planar. The dynamics of the satellite can be described in the co-rotating frame of the Earth-Moon system (Fig. 4) by the equations of the Sun-Earth-Moon bi-circular model:¹⁸

$$\dot{\mathbf{X}} = \begin{cases} \mathbf{v}, \\ -(1 - \mu) \frac{\mathbf{r}_e}{r_e^3} - \mu \frac{\mathbf{r}_m}{r_m^3} - \bar{m}_s \left(\frac{\mathbf{r}_s}{r_s^3} + \frac{\mathbf{s}}{s^3} \right) - Z Z \mathbf{r} - 2 Z \mathbf{v}, \end{cases} \quad [7]$$

where $\mathbf{X} = [\mathbf{r}, \mathbf{v}]^T$, $\mathbf{r} = [x \ y \ z]^T$ is the position vector of the spacecraft as seen from the Earth-Moon barycentre, $\mathbf{v} = [\dot{x} \ \dot{y} \ \dot{z}]^T$ is the synodic velocity vector of the spacecraft and $\mu = M_m/(M_m + M_e)$ is the mass-ratio parameter of the Earth-Moon system. The quantity $\bar{m}_s = M_s/(M_m + M_e)$ stands for the mass of the sun in normalized units (i.e., one unit-length equals the semi-major axis of the Moon's orbit

[†]<https://naif.jpl.nasa.gov/naif/toolkit.html>

3. Trajectory Design

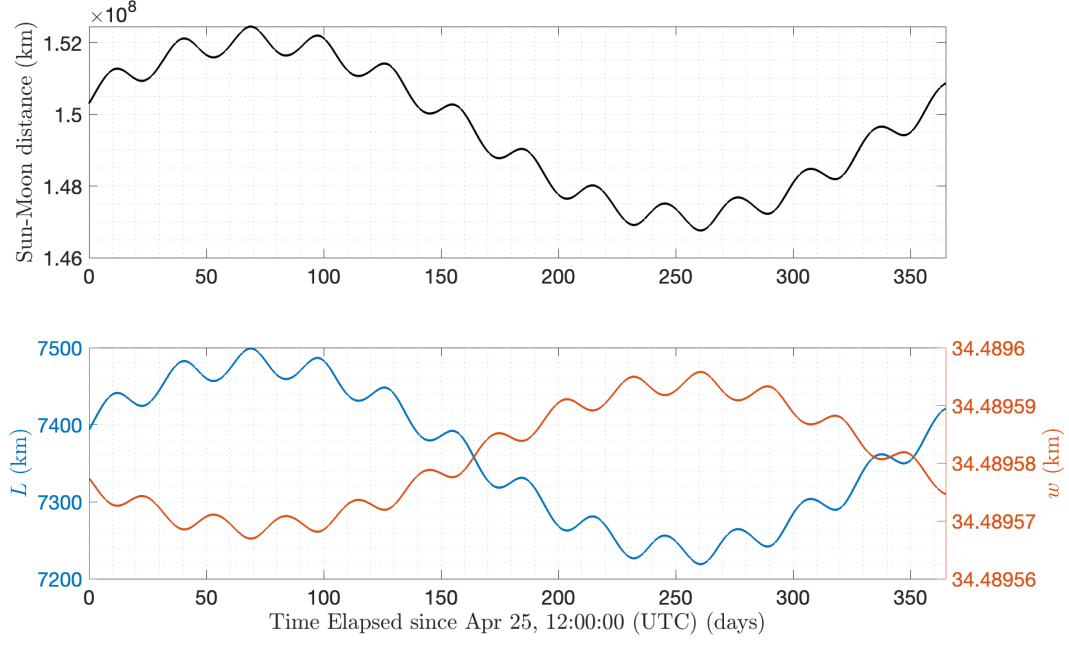


Fig. 3: top) d_{sm} values over one year, starting from Apr 25 2023 at 12:00:00 (UTC); bottom) Changes in the L and w values recorded throughout the same time interval.

about the Earth, namely a_m , one unit of time corresponds to $\sqrt{\frac{a_m^3}{G(M_m + M_e)}}$, and one unit of mass

corresponds to $(M_m + M_e)$. Furthermore,

$$Z = \begin{bmatrix} 0, & -1 \\ 1, & 0 \end{bmatrix}^T, \quad [8a]$$

$$\mathbf{r}_e = \mathbf{r} - [-\mu, \quad 0]^T, \quad [8b]$$

$$\mathbf{r}_m = \mathbf{r} - [1 - \mu, \quad 0]^T, \quad [8c]$$

$$\mathbf{r}_s = \mathbf{r} - \mathbf{s}, \quad [8d]$$

$$\mathbf{s} = a_s [\cos(\theta_s), \quad -\sin(\theta_s)]^T, \quad [8e]$$

$$\theta_s = \omega_s (t - t_0), \quad [8f]$$

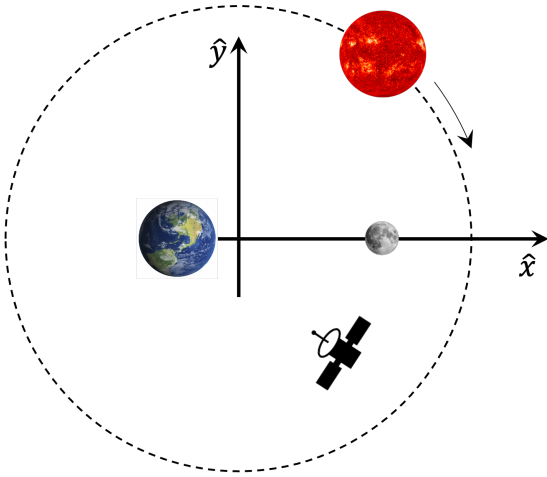


Fig. 4: Schematics of the Earth-Moon-Sun Bi-Circular Problem. Distances are not in scale to ease with the visualization.

where a_s is the semi-major axis of the circular orbit of the Sun as seen from the Earth-Moon barycentre, and ω_s is its mean motion as seen from the co-rotating frame of the Earth-Moon system. It follows that the Eq. [7] represents a non-autonomous system of four first-order ordinary differential equations that depends on four parameters: $\mathbf{p} = [\mu, \quad \bar{m}_s, \quad a_s, \quad \omega_s]^T$. The system may be rewritten in a more compact form as

$$\dot{\mathbf{X}} = \mathbf{f}(t, \mathbf{X}, \mathbf{p}) = \begin{cases} \mathbf{v}, \\ \nabla \mathcal{U}_{eff} - 2Z\mathbf{v}, \end{cases} \quad [9]$$

where

$$\mathcal{U}_{eff}(t, \mathbf{r}, \mathbf{p}) := \frac{(1-\mu)}{r_e} + \frac{\mu}{r_m} + \bar{m}_s \left(\frac{1}{r_s} - \frac{\mathbf{s}^T \mathbf{r}}{s^3} \right) - \frac{1}{2} Z Z^T \mathbf{r}^2 \quad [10]$$

3. Trajectory Design

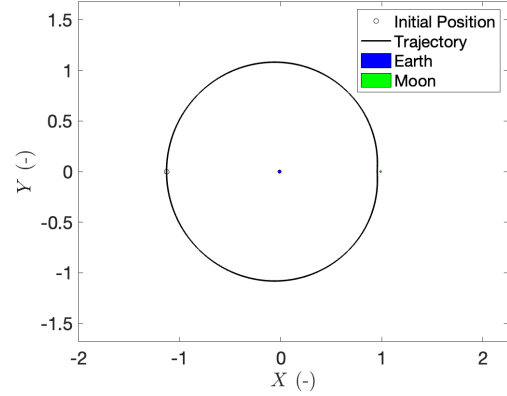
is known as the effective potential.¹⁹ Note that \mathcal{U}_{eff} reduces to the effective potential of the Planar Circular Restricted Three-Body Problem (PCRTBP) whenever \bar{m}_s is set to zero. Accordingly, let us rewrite Eq. [10] as

$$\mathcal{U}_{eff}(t, \mathbf{r}, \mathbf{p}) := \mathcal{U}_{eff}^{PCRTBP} + \epsilon \bar{m}_s \left(\frac{1}{r_s} - \frac{\mathbf{s}^T \mathbf{r}}{s^3} \right), \quad [11]$$

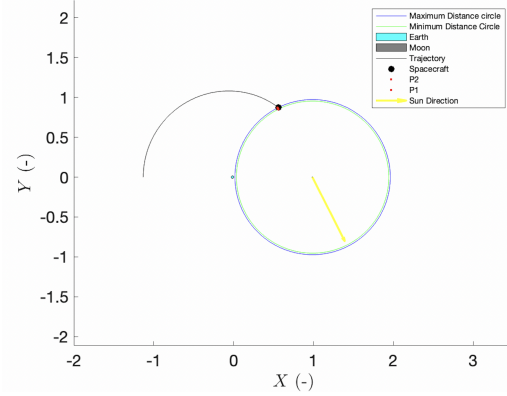
where ϵ is an homotopy continuation parameter $\in [0, 1]$. Whenever $\epsilon = 0$, the equations of motion reduces to the equations of the Earth-Moon PCRTBP. When $\epsilon = 1$, the equations of motion become the ones of the Sun-Earth-Moon bi-circular model as shown in Eq. [9]. This passage is fundamental in calculating SRPOs, as candidate trajectories can be imported from existing databases of PCRTBP periodic orbits ($\epsilon = 0$) that can be found in the literature (e.g.,²⁰ and²¹) and later continued in the bi-circular model ($\epsilon = 1$) of the Sun-Earth-Moon system using pseudo-arclength continuation.²²

Figure 5 introduces the most promising candidate identified so far for a Moon-enabled Sun occultation mission, corresponding to the (2:1) A_1 family member in Ref.²¹ The candidate orbit is imported into the Sun-Earth-Moon BCP and differentially corrected until $\epsilon = 1$. The result of the homotopy continuation approach is shown in Fig. 5a, whereby a fully periodic 2 : 1 SRPO in the Sun-Earth-Moon BCP is portrayed. The orbit is analysed a-posteriori in order to assess whether close passages to the Moon's Sun occultation zone can be detected. This is shown in figure 5b, where the occultation zone is highlighted as the red area between the two concentric circles of radii l_2 and l_1 , respectively. The 2 : 1 trajectory is observed to pass very close to the occultation zone (less than 5000 km to be exact), prompting the application of numerical optimization techniques that can not only introduce the actual dynamics of the Sun-Earth-Moon system, but also guarantee passage through the Moon-enabled Sun's occultation zone via fuel-efficient orbital manoeuvres.

jTOP, a freeware trajectory software developed by Stefano Campagnola and his team, has been adopted for the calculations.²³ jTOP takes as an input discrete points along a candidate trajectory, their epochs in UTC time coordinates, along with forward and backward propagation times between consecutive nodes. Internally, the software propagates the states of the trajectory forward and backward in time using the actual dynamics of the Sun-Earth-Moon system (i.e., time-varying non-coplanar orbits) so as to evaluate the residuals in both time



(a) Fully periodic A_1 2 : 1 SRPO in Sun-Earth-Moon BCP.



(b) Close passage detected during a-posteriori analysis of the A_1 2 : 1 SRPO.

Fig. 5: MESOM candidate trajectory.

and Cartesian coordinates at user-defined patching points. These residuals and their partial derivatives are later passed to SNOPT, a shareware trajectory optimization procedure,²⁴ which nullifies their values in both the space and time domains while adjusting the nodes, epochs, forward and backward propagation times of the candidate trajectory. Additional constraints can be added to ensure passage through the Moon-enabled Sun occultation zone at the candidate occultation epochs recorded in the a-posteriori analysis of Fig. 5b. Figure 6 shows the baseline MESOM trajectory obtained at the end of the optimization procedure in which impulsive manoeuvres have been added to ensure the continuity of the trajectory in both position and time over 15 synodic months.

The extended occultation and ΔV profiles are disclosed in Fig. 8, along with the total and partial eclipse durations due to the Moon and Earth (the

4. Transfer Analysis

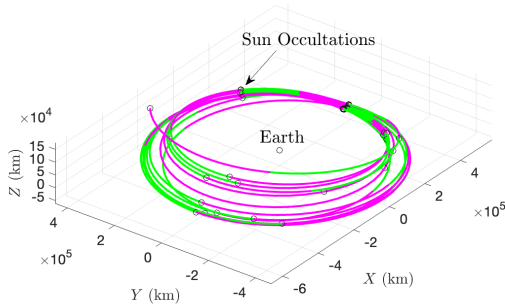


Fig. 6: Optimized A_1 (2:1) SRPO in the real-ephemeris model of the Sun-Earth-Moon system.

orange and blue lines of Fig. 7, respectively). The spacecraft is found to skip a couple of Sun occultation opportunities in favour of a more fuel-efficient orbital plane change, which ultimately place it on a more convenient orbital configuration to resume prolonged sun corona observations. This seems to be confirmed by inspection of the impulsive manoeuvre magnitudes, which appear to be the highest near the shortest duration Sun occultation windows (10th and 11th synodic months). Nevertheless, the spacecraft spends on average 15 minutes inside the Moon-enabled Sun occultation zone of Section 2, reaching peaks of 48 minutes of high-quality observations at the beginning of the mission. The total ΔV cost of the trajectory adds up to 635 m/s, whereas the longest total lunar eclipse is found to be 10.15 hrs.

4. TRANSFER ANALYSIS

A preliminary transfer analysis has been carried out in order to estimate the propellant cost required to insert the proposed spacecraft into the baselined A_1 (2:1) SRPO. As a baseline scenario, MESOM is assumed to be released into a free-return trajectory, one day after the translunar injection manoeuvre.^{25,26} A similar deployment strategy is currently being adopted for piggyback CubeSats onboard the maiden flight of NASA’s Space Launch System.²⁷ Fig. 9 displays the free-return trajectory utilized for our investigations, as well as the deployment point along the transfer trajectory.

Starting from the deployment point of Fig. 9, an impulsive manoeuvre ΔV_1 is added in order to venture into the cislunar environment and eventually insert into the candidate SRPO. To achieve this goal, the apogees of any forwardly propagated tra-

jectory are extracted and compared with a database of Earth apogees obtained from the backward propagation of 4000 trajectories along the stable manifold of the (2:1) synodic resonant orbit. The stable manifold of the (2:1) synodic resonant orbit was generated using standard procedures of dynamical systems theory as explained in Ref.²⁸ A picture of the in-plane location and Sun phase angle values obtained at the apogees of the *backwardly* propagated trajectories is offered in Fig. 10. The goal is to patch the forwardly propagated trajectory after ΔV_1 with a backwardly propagated one near any of these candidate “patching points”, thus obtaining a continuous transfer in position and time (i.e., the values of the sun phase angle).

A multi-objective trajectory optimization was run in MATLAB using its genetic algorithm optimizer to find an initial Sun phase angle σ_0 and ΔV_1 values that would minimize either the time-of-flight or total propellant cost of the transfer. Patching opportunities were considered if and only if the relative position error at the patching point was less than 10 000 km and the difference in the instantaneous Sun phase angle value between the forwardly and backwardly propagated legs was less than 1 degree. The Pareto front obtained from this analysis is disclosed in Fig. 11 and enables selection of a good compromise between the total ΔV cost and time-of-flight of the transfer.

Once a reliable initial guess has been identified, a final trajectory optimization procedure can be implemented to nullify the residuals in the spacecraft’s position and Sun phase angle at the patching point while minimizing the total propellant cost of the transfer. MATLAB’s *fmincon* has been utilized for this purpose, yielding the fully optimized transfer trajectory of Fig. 12. The spacecraft executes an initial impulsive manoeuvre of $\Delta V_1 = 94.97$ m/s before fly-bying with the Moon and venture into the vicinity of the Earth-Moon system (the green leg of Fig. 12, corresponding to the forwardly propagated leg of the transfer). After 36.6577 days, the spacecraft reaches the optimized patching point and executes a second impulsive manoeuvre of $\Delta V_2 = 96.31$ m/s to insert into a stable manifold trajectory of the (2:1) SRPO. Here, the chaotic dynamics of the Sun-Earth-Moon Bi-Circular Problem naturally drives the spacecraft towards the desired science orbit (magenta line of Fig. 12), where it would eventually begins its scientific investigations. The total time-of-flight of the transfer adds up to 249.9378 days. Thanks to the stable manifold approach, no additional impulsive manoeuvres are required in order to insert the satellite into

4. Transfer Analysis

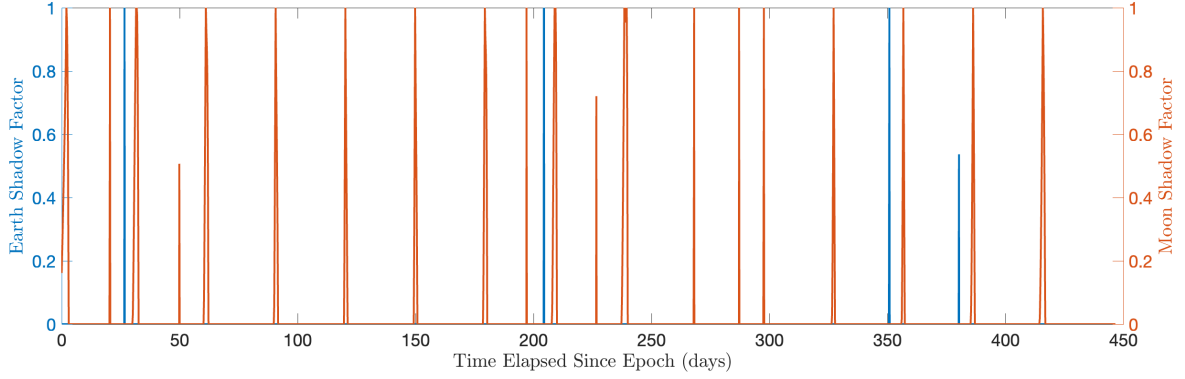


Fig. 7: Total and partial eclipses due to the Moon (orange line) and Earth (blue line)

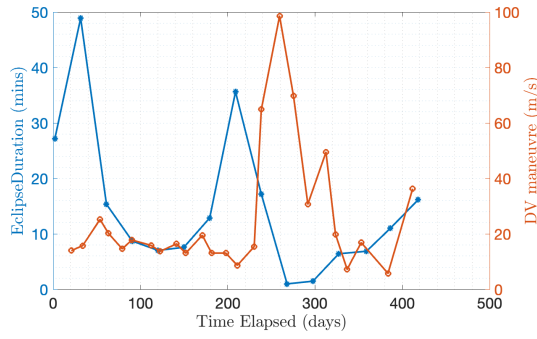


Fig. 8: Time spent in the occultation zone and impulsive manoeuvres extracted from the A_1 (2:1) SRPO optimized over 15 synodic months.

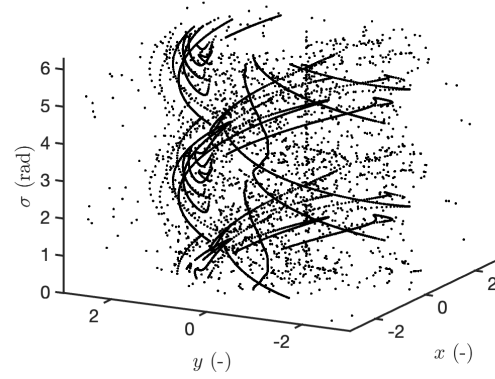


Fig. 10: Earth's apogees obtained from the backward propagation of the (2:1) SRPO stable manifold for different Sun phase angle values.

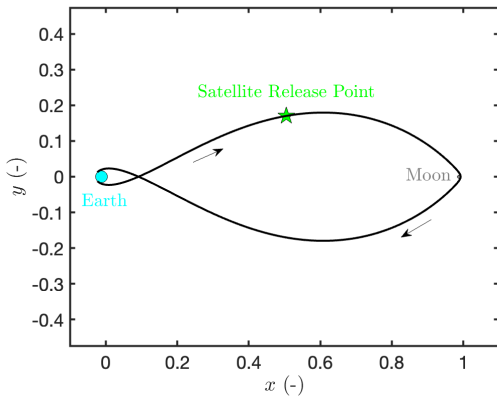


Fig. 9: Free-return trajectory being simulated for the transfer analysis. The spacecraft is released one day into the translunar orbit

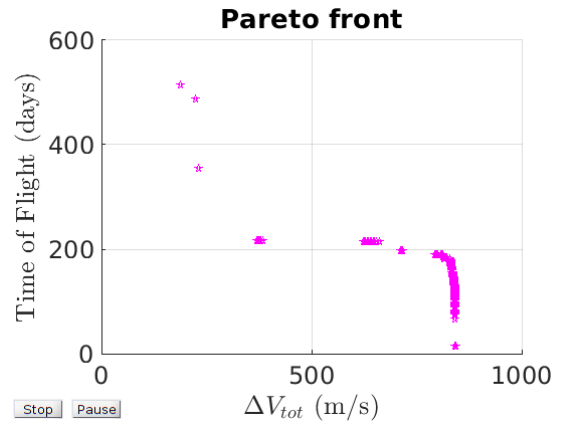


Fig. 11: Top) Pareto front generated with the multi-objective optimizer run in MATLAB. Bottom) Candidate initial guess for the transfer trajectory.

the final (2:1) SRPO. The orbit injection manoeuvre would remain minimal even if the transfer trajectory

5. Science Payload

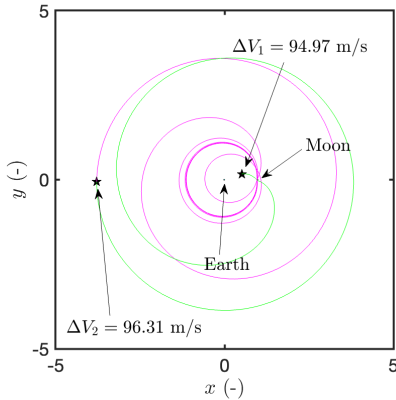


Fig. 12: Re-optimized transfer trajectory obtained with MATLAB’s `fmincon`. Two impulsive manoeuvres enable the spacecraft to first flyby the Moon (green leg) and eventually connect with the stable manifold (magenta line) of the candidate (2:1) SRPO.

is re-analyzed and re-optimized in the full-ephemeris model of the Sun-Earth-Moon system. This brings the estimated ΔV cost of the MESOM mission (transfer plus 15 synodic months) up to approximately 850 m/s.

5. SCIENCE PAYLOAD

5.1 Primary Payload

Solar observations have been made in space using coronagraph systems, as for example used on the joint European Space Agency and National Aeronautics and Space Administration Solar and Heliospheric Observatory (SOHO) spacecraft.²⁹ The Large Angle and Spectrometric Coronagraphs (LASCO) block direct light from the photosphere with internal and external occulters, creating a permanent artificial eclipse and enabling corona observations from 1.5 to 30 sun radii.³⁰ The LASCO suite, comprising 3 coronagraphs, consumes nearly 100 W of electrical power and the optical instruments occupy a 135 cm × 34 cm × 32 cm volume and have a mass of 21 kg.³¹

The Naval Research Laboratory (NRL) has more recently produced a Compact Coronagraph (CCOR) for the Geostationary Operational Environmental Satellite (GOES)-U, launched in June 2024.³² The CCOR instrument has a mass of 25 kg, and occupies a volume of 90 cm × 54 cm × 39 cm, making it suitable for mounting on a low-cost platform such as the SSTL-150 class[‡] or similar.

[‡]<https://rsdo.gsfc.nasa.gov/images/catalog/SSTL150.pdf>

One advantage of a coronagraph instrument for the MESOM spacecraft is that it does not need an artificial occulting disc as it uses the Moon as a natural occulter. The telescope arrangement can be shorter than conventional space-based coronagraphs and based on a heritage of total eclipse instrumentation, thus at a ground-based TRL of 9. Figure 13 illustrates four of such instruments, including a broadband visible polarizing imager that will give high resolution images of the solar atmosphere from very close to the photosphere to large distances (8 sun radii), thereby enabling studies of fine-scale magnetic structures and their connection to the Sun,^{33,34} and a multi-channel spectrometer that will provide high spectral resolution data of the Fe emission lines, giving line-of-sight velocities, and non-thermal broadening diagnostics.³⁵ Preliminary mass and power estimates of 20 kg and $\simeq 30$ W will be allocated for the MESOM’s primary instrument. Data rate would vary between a few Kbps to a few Mbps following Moon-enabled Sun occultations.

5.2 Secondary Payload

The MESOM spacecraft may also carry particle detectors to give a full picture of space weather conditions. In 2004, the Surrey Space Centre (SSC), working in collaboration with Mullard Space Science Laboratory (MSSL), carried out a survey of scientific instruments for a proposed space weather monitoring mission. Figure 14 shows the instrument characteristics found at that time, along with their technological maturity. More recent work has highlighted the need for more and better measurements of solar energetic particles in interplanetary space with the aim understanding their origin and their transport away from the Sun, which is highly complex. New miniaturized instruments have been developed under ESA and UKSA funding, including the High Energy Particle Instrument,³⁹ which offers high capability in a small package (<1 kg) and can extend the measurement energy range right up to 1 GeV and beyond. MESOM offers the opportunity to deploy this type of instrument to enable a new scientific investigation of solar energetic particles in near-Earth interplanetary space, but avoiding the complications of attempting such measurements from within the magnetosphere. It can also provide a space weather observatory to enable and improve nowcasting and forecasting for lunar and terrestrial operations. Accordingly, a similar mass of $\simeq 20$ kg and power of $\simeq 30$ W can be allocated for these secondary payloads, along with

– Accessed on Mar 29, 2022

5.2 Secondary Payload


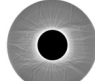
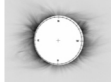
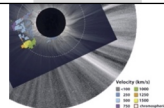
	Name	Main science diagnostic	Example data
HiBri	High-resolution Broadband imager	Magnetic field structure at large and small scales CME structure, initiation, evolution Sources, causes, and propagation of small-scale dynamic events including magnetic switchbacks	
CIP	Coronal Imaging Polarimeter	Electron density: inversions, tomography, density of CMEs etc.	
NaBLIS	NarrowBand Line Imager Suite	Ion density Electron temperature Freeze-in distances	
CHiLS	CHiLS: Coronal High-resolution Line Spectrometer	Ion density & temperature Electron temperature Non-thermal widths Bulk plasma motions	

Fig. 13: Candidate MESOM Primary Instruments. The image in the top row represents the type of high-resolution imagery that may be collected by HiBri. This 2023 total eclipse image is courtesy of Starha, Habbal, and Druckmuller[§]. The image in the second row is reproduced from Ref. 36. The image in the third row is from Ref. 37. The image in the bottom row is from Ref. 38.

Instrument	Mass (kg)	Power (W)	Status	Main references	Size (cm)
Solar and galactic radiation monitor	6	8	2	GOES, Ulysses	20x20x20
Solar Wind monitor	6	5	2	ACE, AMPTE, Giotto, Cassini, Cluster	20x20x20
Thermal plasma monitor	6	8	2	AMPTE, CRRES, Cluster, Cassini	20x20x20
Mid energy particle monitor	2	4	2	CRRES, Polar, Cluster, GOES, Hitchhikers	15x15x15
Magnetometer	1	2	1	Cluster, Rosetta	20x10x5 (elec) 4x4x4 (2 sensors on boom)
Low energy plasma monitor	2	4	2	UARS, Cluster, Rosetta	15x15x15

Fig. 14: Candidate instrument properties. Under status, we indicate the maturity of instruments as follows: 1=off the shelf, 2=to be adapted from existing designs, 3=need further development, but technology exists, 4=need for technological development, 5=feasibility to be proven.

6. Spacecraft Bus

a total volume of $20 \text{ cm} \times 90 \text{ cm} \times 20 \text{ cm}$, to sit alongside the main telescope(s). The data rate for these additional instruments should be on the order of $\simeq 100 \text{ Kbps}$.

6. SPACECRAFT BUS

Given the science payload instruments discussed in the previous Section, the SSTL Geostationary Minisatellite Platform (GMP) was selected as a good candidate platform for the MESOM spacecraft. Designed for low cost-of-entry for GEO/MEO missions with a 5-7 year lifetime (c.f., Fig. 15), the GMP-D platform was first flown on the GSTB-V2/A (Giove-A) mission, launched on December 28, 2005.⁴⁰ Its specifications can be found in Table 1.

The GMP-D bus has a maximum payload mass capability of 110 kg and a power capability of $\simeq 1 \text{ kW}$, i.e., well above the estimated payload power and mass budget of 40 W and 40 kg, respectively. A telescope similar in size to NRL's CCOR could be carried along with a number of smaller radiation monitoring payloads and for a total combined volume of $90 \text{ cm} \times 80 \text{ cm} \times 60 \text{ cm}$ on the top of the Payload Frame ($130 \times 130 \text{ cm}^2$). All of the instruments will be insulated with Multi-layer insulating blanket (MLI), while the coronagraph will have a radiator at the back facing away from the Sun when in operation.

The tanks shown in Fig. 15 can hold 90 litres of propellant and occupy most of the propulsion bay along with the reaction wheels and solar array drives (SADs). Next to SADs are the avionics plates that carry all the necessary platforms systems to operate the spacecraft. The payload frame is adaptable to the needs of the individual payloads and its in-depth design is left for the future phases of the project.

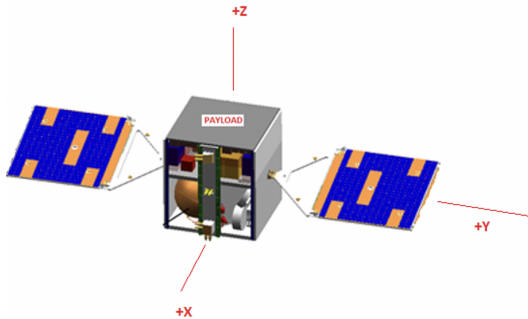


Fig. 15: Illustration of the SSTL GMP-D Platform System Diagram. The baseline design of MESOM envisages a external payload allocation on the top of the upper frame.

It is highlighted that the GMP platform has been obsolete for a number of years and ultimately replaced by what is now known as the SSTL-Mini platform[¶]. The numbers of Table 1 will be updated accordingly during future phases of the project and through the direct involvement of satellite manufacturers.

7. PROPULSION SYSTEM

The propulsion system selection was focused on chemical propulsion options as impulsive-type manoeuvres were so far considered for the design of the MESOM baseline trajectory. The ArianeGroup Mono-Methyl Hydrazine (MMH)/Mixed Oxides of Nitrogen (MON) 10 N liquid bipropellant engine has been selected as the baseline thruster for the delta-v delivery envisioned by the orbital analyses. Bipropellant engines combine a fuel and an oxidiser in a combustion chamber where they react to form reactants products and heat. The hot gaseous products are then expanded through a nozzle. The overall propulsion architecture is dual-mode and incorporates 4 MMH/MON 10 N liquid bipropellant engines^{**} for delta-v delivery and 6 MMH 1 N monopropellant thrusters^{††} for attitude control. A picture of the two candidate devices is disclosed in Fig. 16, whereas Tables 2 and 3 summarize the capabilities of the orbital and attitude control engines, respectively.



Fig. 16: Left) ArianeGroup's 10 N bipropellant thruster. Right) ArianeGroup's 1 N Hydrazine Monopropellant Thruster.

Considering a reference specific impulse of 290 s and a dry mass of 240 kg, the estimated propellant mass of the spacecraft can be calculated as a function the representative delta-V range of the sun occultation mission. Key performance parameters are sum-

[¶]<https://www.sstl.co.uk/getmedia/94ebb49a-b135-40f4-b2be-4670de7e54a7/SSTL-MINI.pdf>

^{**}<https://www.space-propulsion.com/spacecraft-propulsion/bipropellant-thrusters/10-bipropellant-thrusters.html>

^{††}<https://space-propulsion.com/brochures/hydrazine-thrusters/hydrazine-thrusters.pdf>

7. Propulsion System

Table 1: Specifications of the SSTL GMP-D platform selected for the strawman MESOM mission concept.

Dimensions:	1.3 m x 1.3 m x 1.4 m (stowed)
Payload Mass:	up to 110 kg (GMP-D)
Wet Mass:	up to 400 kg
Electrical Power:	up to 1 kW
Propellant:	Hydrazine Mono-Propellant or MMH/NTO Bi-Prop.
Attitude Control:	Reaction Wheels and Thrusters
Pointing Accuracy:	Roll/Pitch ± 0.1 deg (3σ); Yaw ± 1.0 deg (3σ)
Battery:	Lithium-Ion sized to eclipse conditions
Solar Arrays:	Triple-Junction solar cells; deployed, tracking panels.

Table 2: ArianeGroup’s MMH/MON 10 N engine specifications.

Application	delta-v delivery
Propellant (fuel/oxidiser)	MMH/MON
Thrust nominal (range)	10 N (6 – 12.5 N)
Specific Impulse	292 s
Flow rate nominal (range)	3.5 10-3 kg/s (2.3 – 4.2 10-3 kg/s)
Mixture ratio nominal (range)	1.6 (1.2 – 2.10)
Inlet Pressure Range	10 – 23 bar
Chamber pressure	9 bar
Expansion ratio	150
Throat diameter	2.85 mm
Nozzle Exit Diameter	35 mm
Thruster mass (including dual seat valve)	650 g
Chamber Nozzle Material	Platinum/Rhodium Alloy
Qualified Longest single burn	8 hours
Qualified accumulated burn life	69 hrs
Qualified cycle life	1,100,000 cycles

Table 3: ArianeGroup’s MMH 1 N engine specifications.

Application	Attitude Control
Propellant	Hydrazine
Thrust nominal (range)	1 N (0.32 – 1.1 N)
Specific Impulse	220 s
Minimum impulse bit	0.01 – 0.043 Ns
Flow rate nominal (range)	0.44 10-3 kg/s (0.142 – 0.447 10-3 kg/s)
Inlet Pressure Range	5.5 – 22 bar
Thruster mass (including valves)	290 g
Nozzle expansion ratio	80
Single burn life	12 hours
Accumulated burn life	50 hrs
Cycle life	59,000 cycles
Number of cold starts	10

marized in Table 4, including the propellant masses for both the transfer and science orbit phases, as well as the oxidiser and fuel masses and volumes. Assuming tanks of equal size, and based on the larger oxidiser volume, we can estimate a qualified propellant

volume for the tanks selection of 42 L, accounting for a 5% trapped propellant volume and 2% ullage volume. An estimate of the overall inert mass of the propulsion system is provided in Table 5, along with a breakdown of the different components.

8. Comms & Link Budget Analysis

Table 4: Propellant mass and volume calculations for the Sun occultation mission.

Thruster	10 N Bipropellant Engine
Number of Thrusters	4
Thrust (single thruster)	10 N
Specific Impulse	290 s
Nominal Propellant mass – total	83.6 kg
Nominal Propellant mass – transfer	22.0 kg
Nominal Propellant mass – scientific phase	61.6 kg
Total propellant mass including a 10% margin	92 kg
Oxidiser mass	56.6 kg
Fuel mass	35.4 kg
Oxidiser volume	39.2 L
Fuel volume	35.4 L

Table 5: Overall inert mass of the propulsion system envisioned for the MESOM spacecraft

Item	Mass	Note
Delta-v thrusters (bipropellant)	2.6 kg	ArianeGroup 10 N bipropellant (4 thrusters)
Attitude thrusters (monopropellant)	1.74 kg	ArianeGroup 1 N monopropellant (6 thrusters)
Tank fuel	6 kg	Based on Northrop Grumman catalogue ^{††} . Operating pressure \simeq 20 bar
Tank oxidiser	6 kg	Based on Northrop Grumman catalogue. Operating pressure \simeq 20 bar
Pressurant gas and tank	6 kg	Volume: 15.7 L. Operating pressure: 248 bar. Based on Northrop Grumman catalogue.
Pipes, valves, regulators, transducers etc	5 kg	
Propulsion system inert mass estimate	27.3 kg	
Inert mass fraction	23%	

Regarding the propellant mass needed for the attitude control requirements using monopropellant thrusters, an accurate estimate will be assessed at a later phases of the MESOM project. In the meantime, a 10% fuel overestimate (\simeq 9 kg) is already being included in the budget above along with additional \simeq 10 L qualified propellant volume. The margins being allocated can potentially provide an additional \simeq 10 kg of hydrazine propellant for attitude control manoeuvres.

8. COMMS & LINK BUDGET ANALYSIS

The key functionalities of a communication subsystem have been explored for an S or X-band system for direct-to-Earth communication (DtE) at 22.4 dBW to provide 1) Telemetry, Tracking & Command (TTC) or data downlink and 2) support RF ranging capabilities. Relevant constraints are DtE –

CCSDS^{§§} 401.0.B-30 with Classical Coding: Conv. R=1/2, K=7 R.S. (255,223) at 5.3 dB and RF Ranging – CCSDS 414.1.B-2, 415.1.B-1, assuming a sample rate of 0.2 Msps (millions of samples per second). S-band is not recommended due to ESTRACK stations^{¶¶} moving to only X and Ka-band services, but explored as U.K. facilities may be available for the MESOM spacecraft.

A custom-made python script that calculates the gain-to-noise-temperature ratio (G/T) over time was used to account for the orbital motion of the MESOM spacecraft and specify the system requirements relating to the spacecraft, payload and ground segment. In the G/T method, the gain of the receive antenna (G) is compared to the system noise temperature (T) to determine whether the signal to noise ratio (SNR) is sufficient for communicating with the

^{§§}Consultative Committee for Space Data System Standards

^{¶¶}<https://directory.eoportal.org/web/eoportal/satellite-missions/content/-/article/estrack>

spacecraft.⁴¹ In the DtE simulations, an ITU atmospheric model is used to accurately represent attenuations. The ITU-P 676-11 Standard is implemented by means of Surrey Space Centre - OnBoard Data Handling group's modelling tools that account for different signal losses. Worst case scenarios are assumed for both the S-band at 2290 MHz and the X-band at 8500 MHz, respectively (c.f., Fig. 17). In addition, Imbriale's paper⁴² is used to estimate antenna noise temperatures of 134 K at S-band and 19 K at X-band to potentially account for the Moon in the field of view (worst case scenarios).

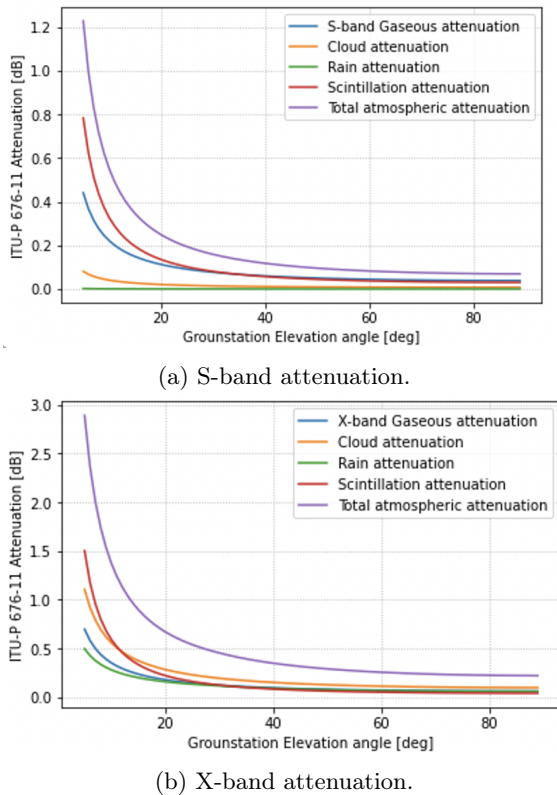


Fig. 17: Implementation of ITU-P 676-11 Standard for DtE Analysis.

Figure 18 illustrates the calculated (G/T) values for a proposed 10 W Radio Frequency (RF) output power and 200 kbps. Although these values can—and should be—modified when more details on the MESOM's concept of operations (CONOPS) become available, they were chosen to ensure a positive link margin with available room for Eb/N0 to operate at a known minimum (e.g., 2 dB). The main findings are that X-band direct-to-Earth communications are possible with 10 W power and 0.2 Mbps and 2 Msps for TTC and ranging activities, respectively. The Goon-

hilly Earth Station (GHY6) has a worst-case G/T of 46.03 dB/K.

Starting from the G/T values of Fig. 18, the communications link status over the mission duration can be derived as shown in Fig. 19. Here, positive link margins (i.e., greater than 2 dB) are shown in green, whereas link margins lower than 2 dB margin are shown in yellow. Red areas denote no line of sight (LOS) due to Earth or Moon occultations, which prevent any communication with the satellite.

For X-band DtE and ranging, there are two options applicable to the sun occultation mission: the IMT M-ARGO Transponder⁴³ and existing Syrlinks ECW27 and N-XONOS X-band transmitter systems. The M-ARGO transponder is requiring 1.3 Units of volume ($1U = 10^3 \text{ cm}^3$, excluding interfacing requirements), with an estimated mass of 1.35 kg. The Syrlinks systems shown are transmitters only and consume approximately the same mass / volume as the M-ARGO system transmitter at a lower volume and mass requirements (0.4 U and 0.4 kg, respectively).

For X-band antennas, there are two options available from Syrlinks: X-T2 and X-T3. Both have flight heritage and need further modification to meet the higher 8.5 GHz frequency from the current 8 – 8.4 GHz range. Further discussions will be required in the next phases of the MESOM project to choose either the IMT M-ARGO transponder or a Syrlinks derived product along with suitable X-band or S-band antennae. The OBDH Group is in parallel developing an X-band RF transponder and antennas towards Lunar applications from LEO developments.⁴⁴

9. THERMAL DESIGN AND CONTROL

Spacecraft thermal design requires careful attention due to the potentially long eclipses experienced throughout the preliminary MESOM trajectory. As a result, the appropriate choice of structural materials and mountings to control conduction, as well as the appropriate selection of the thermo-optical properties of surfaces to control radiation – all of which form part of a passive thermal control strategy – become crucial for the success of the mission. In addition, active thermal control techniques (such as the use of heaters) are required to maintain the spacecraft and its systems within operational temperature limits.

A preliminary thermal mathematical model (TMM) of the spacecraft was set up to predict its thermal behaviour, and to examine the effects of different thermal control strategies. The spacecraft is assumed as being composed of a number of discrete regions within which temperature gradients can be

9. Thermal Design and Control

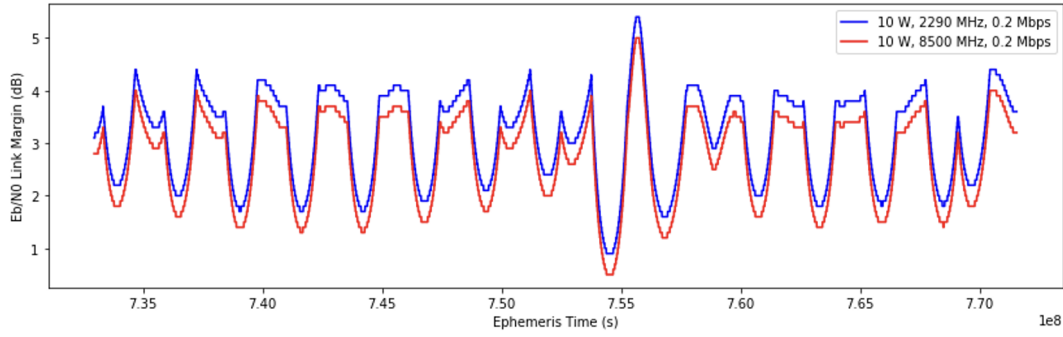


Fig. 18: RF DtE Analysis (G/T).

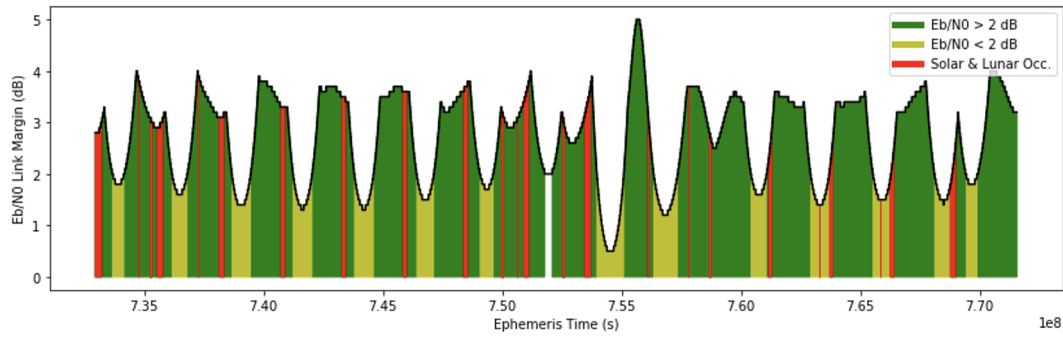


Fig. 19: Link Budget of X-band Communications to Earth. Similar plots can be drawn for the S-Band DtE link budget.

neglected. These regions are known as “isothermal nodes”. Each node is characterized by a temperature, thermal (heat) capacity, heat dissipation, and radiative and conductive interfaces with surrounding nodes. Nodes that can “see” space directly will also have radiative interfaces with the external environment (Sun, Moon, space). For surfaces in direct contact, Fourier’s Law of Conduction applies:

$$Q_c = h_c \Delta T, \quad [W] \quad [12]$$

where h_c is the thermal conductance (which depends on material conductivity, surface area of contact and thermal path length) and ΔT is the temperature difference (in kelvin) between the two surfaces.

For a spacecraft composed of “n” isothermal nodes, the rate of heat flow conducted from the i th to the j th node is:

$$Q_{cij} = h_{ij} (T_i - T_j), \quad [13]$$

where h_{ij} is the effective conductance between the nodes i and j , and T_i , T_j are the temperatures of nodes i and j , respectively.

For diffuse surfaces, the amount of radiation leaving a surface i and absorbed by a surface j is

$$Q_{rij} = A_i F_{ij} \epsilon_{ij} \sigma (T_i^4 - T_j^4), \quad [14]$$

where A_i is the area of surface i , F_{ij} is the view factor of surface j as seen from surface i , and ϵ_{ij} is the effective emittance.

If the mass and specific heat of the node i are m_i and C_i , respectively, the heat balance equation for node i can be written as

$$\begin{aligned} m_i C_i \frac{dT_i}{dt} = & Q_{ext,i} + Q_i - \sigma \epsilon_i A_{space,i} T_i^4 + \dots \\ & - \sum_{j=1}^n h_{ij} (T_i - T_j) + \dots \\ & - \sigma \sum_{j=1}^n A_i F_{ij} \epsilon_{ij} (T_i^4 - T_j^4), \end{aligned} \quad [15]$$

where $A_{space,i}$ is the effective area with an unobstructed view of space, and Q_i is the internal heat dissipation. Furthermore, the external heat input is given by

$$Q_{ext,i} = J_s \alpha_i A_{solar,i} + J_\alpha \alpha_i A_{albedo,i} + J_p \epsilon_i A_{planetary,i}, \quad [16]$$

where

- J_s is the solar radiant flux impinging on the surface;

9.1 Case 1: Heat Balance of the Deployed Solar Panels - Sun Pointing

- α_i is the solar absorptivity;
- $A_{solar,i}$ is the effective (projected) area receiving direct solar radiation;
- J_α is the albedo flux impinging on the surface;
- $A_{albedo,i}$ is the effective area receiving lunar or terrestrial reflected solar radiation;
- J_p is the IR flux impinging on the surface;
- ϵ_i is the IR emissivity (same as the IR absorptivity);
- $A_{planetary,i}$ is the effective area receiving lunar or terrestrial emitted IR radiation;

With the equations above, an n node model of the spacecraft can be set up, and the resulting heat balance equations solved via the Finite Difference Method (FDM).⁴⁵ The model was run for different mission scenarios, and the results are checked to see if the predicted temperatures remain within safe limits.

The assumed effective specific heat capacity of the MESOM spacecraft is that of aluminium alloy: $883 \text{ J kg}^{-1} \text{ K}^{-1}$. Combined with an estimated dry mass of 254 kg (c.f. Section 11), the “average” heat capacity of the satellite turns out to be 226 kJ K^{-1} .

The satellite body dimensions are $130 \text{ cm} \times 130 \text{ cm} \times 140 \text{ cm}$ and the payload is $80 \text{ cm} \times 90 \text{ cm} \times 60 \text{ cm}$, with the payload mounted on the top of the spacecraft body, as shown in Fig. 15 (+Z facet). The spacecraft deploys two $100 \text{ cm} \times 100 \text{ cm}$ solar panels from the +Y and -Y facets, each carrying 234 solar cells. The +X facet is nominally pointing towards the Sun during science operations.

Based on the aforementioned spacecraft configuration, the internal power dissipation is assumed to vary as summarized in Tab. 6. The desired temperature limits within the spacecraft are 10° C (lower) and 40° C (upper). The maximum eclipse duration observed during the trajectory design analyses was found to be approximately 10 hours, separated by long and prolonged periods where the spacecraft is fully impinged by solar radiation.

Note that the thermal IR flux received from the Moon or the Earth, as well as their albedo radiations, will be considered as negligible when compared to the solar heat and internal power dissipations. It follows that the Earth and the Moon can be practically discarded for the preliminary thermal balance analyses of the MESOM satellite.

9.1 Case 1: Heat Balance of the Deployed Solar Panels - Sun Pointing

The deployed solar Panels are assumed to be Sun tracking. Each panel is $100 \text{ cm} \times 100 \text{ cm} \times 1 \text{ cm}$ thick AlBeMet AM162 / aluminium alloy honeycomb. The total mass of each panel adds up to 12 kg , without including an embedded resistive heater of 20 W that can facilitate the thermal control.

The front surface is recommended to be orange Kapton on an aluminium/AlBeMet substrate with 234 triple junction solar cells arranged as 13 strings of 18 (approx. $45 \text{ V @ } 6\text{A}$). Conversely, the back surface is assumed to be carbon impregnated black Kapton.

Assuming that the deployed panels are thermally isolated from the body of the spacecraft, the heat absorbed by each deployed panel adds up to

$$\alpha_s A \phi = 1106 \text{ W}, \quad [17]$$

where $\alpha_s = 0.81$ is the absorptivity of the front of the solar panel. The value of 0.81 is obtained by noting that 29% of the front area $A = 10^4 \text{ cm}^2$ is made of an orange Kapton substrate ($\alpha_s = 0.60$), whereas the remaining 71 % is covered by triple junction cells ($\alpha_s = 0.90$).

At equilibrium, the heat absorbed by the solar panels is balanced by the heat losses. Assuming a back and front panels emissivity of $\epsilon_b = 0.81$ and $\epsilon_f = 0.77$, respectively, the operating temperature of the panel is found to be 60.2° C . This is well within the operational limits of the solar panel and should lead to efficient power generation under full sunlight.

Covering the back panel with 50:50 stripes of black Kapton and first surface vacuum deposited aluminium (VDA) on Kapton gives an emissivity value of $\epsilon_b = 0.43$, resulting in a temperature at equilibrium of $T = 84^\circ \text{ C}$. This is still acceptable and will reduce the heat loss rate in the deep, long period eclipses envisioned before, during, and after the sun occultation observations. In the following, a black/VDA 50:50 striped pattern configuration is considered as the baseline for the MESOM spacecraft’s solar panels.

9.2 Case 2: Heat Balance of the Deployed Solar Panels - 10 hours Total Eclipse

In eclipse, the temperature of the deployed panels will fall. The heat capacity is relatively small ($\approx 12 \text{ kJ K}^{-1}$), despite the use of AlBeMet AM162 alloy, due to the relatively small mass of the solar panels (12 kg). This means that the initial loss of heat amounts to 0.09 K s^{-1} .

9.3 Case 3: Heat Balance of the Spacecraft Body - Payload Sun Pointing (Nominal)

Table 6: Internal Power Dissipations being considered for the MESOM spacecraft

Absolute Minimum:	22 W	(PWR, OBC, TTC & Rx. only)
Payload Off No Comms:	46 W	(Bus Systems Only)
Mode 1: Full Sun / Min. Ops	70 W	(Particles and Fields Payloads)
Mode 2: Ops / No Comms	110 W	(Active Payloads - no heaters)
Mode 3: Ops / No Comms	279 W	(Active Payloads - with heaters)
Mode 4: Data downlink in Full Sun	132 W	(Comms Mode)

If we take -100°C as the minimum acceptable temperature, then additional heating is required. The heat emitted at 173 K (corresponding to -100°C) is approximately 61 W, implying that 60 W heater power per panel would be required to maintain the temperature during the prolonged total eclipses.

Figure 20 illustrates the rate of cooling over 10 hours of eclipse, with and without the effect of adding a 60 W heater. In practice, there will be an additional small heating effect from the thermal IR emissions of the spacecraft body.

Time / minutes	Temperature / $^\circ\text{C}$	Rate of Change of Temperature / K s^{-1}	Temperature / $^\circ\text{C}$ with 60 W heater
0	84.0	-0.092	84.0
15	1.2	-0.032	5.6
30	-27.6	-0.021	-20.6
45	-46.1	-0.015	-36.8
60 = 1 hour	-59.6	-0.012	-48.2
75	-70.2	-0.010	-56.7
90	-78.8	-0.008	-63.4
105	-86.1	-0.007	-68.8
120 = 2 hours	-96.9	-0.006	-73.2
150	-107	-0.005	-80.5
180 = 3 hours	-115	-0.004	-85.5
210	-121	-0.004	-89.1
240 = 4 hours	-126	-0.003	-91.8
300 = 5 hours	-137	-0.002	-95.8
360 = 6 hours	-144	-0.002	-97.9
420 = 7 hours	-150	-0.001	-99.1
480 = 8 hours	-155	-0.001	-99.8
540 = 9 hours	-159	-0.001	-100.2
600 = 10 hours	-162	-0.0008	-100.4

Fig. 20: Solar panel temperature VS time in lunar eclipse, with and without heaters.

We conclude this subsection by highlighting that care should be taken when transitioning from cold eclipses to full sunlight conditions. Solar cells will be particularly cold and prone to generate power surges that can be destructive to the power system. Strings need to be switched out until the panel has warmed up, and the cells have returned to normal efficiency.

9.3 Case 3: Heat Balance of the Spacecraft Body - Payload Sun Pointing (Nominal)

It is assumed that the +X and -X facets of the spacecraft comprise a $130 \text{ cm} \times 140 \text{ cm}$ panel which is covered in Multi-Layer Insulator (MLI) blanket. MLI comprises multiple layers of doubly aluminised Kapton—to cut down radiative heat transport—, separated by layers of Dacron netting—to cut down conductive heat transport.

With an aluminised black Kapton outer layer, the MLI surface α_{MLI} and ϵ_{MLI} values are typically equal to 0.85 and 0.81, respectively. However, the practical emissivity is much lower, given that the MLI acts as a barrier to radiation transmission. For a five-layer MLI, an effective emissivity of 0.03 has been observed. This value drops to 0.015 for a ten-layer MLI. As a result, the heat flow through the MLI is very small and can be safely ignored. Indeed, MLI have been extensively adopted in space exploration to retain heat against the cold blackness of Space.

Similarly to the emissivity, the effective absorptivity of an MLI covered plate is also significantly different from its actual nominal value. In this case, α_{eff} can be estimated as the product between the effective emissivity, ϵ_{eff} , and the α/ϵ ratio. For black Kapton MLI, this gives an effective solar absorptivity of $\alpha_{eff} = 0.03$.

Similarly to the +X facet, the +Y and -Y facets are also $130 \text{ cm} \times 140 \text{ cm}$ panels which are partially covered in MLI blanket. However, the +Y and -Y facets are also envisaged with a radiator section corresponding to either the Avionics Bay or Payload Bay. The radiator comprises a $130 \text{ cm} \times 10 \text{ cm}$ panel of silver-Teflon (Ag-PTFE) second-surface mirror (SSM) Optical Solar reflector (OSR) material of solar absorptivity, $\alpha_s = 0.09$ and emissivity, $\epsilon_s = 0.60$.

The -Z facet ($130 \text{ cm} \times 130 \text{ cm}$) is covered in black-Kapton MLI and also houses the attach fitting. In contrast, the +Z facet ($130 \text{ cm} \times 130 \text{ cm}$) is also covered in black Kapton MLI, but here the external payload box is also mounted. The Payload Box is 90cm (X), 80 cm (Y) and 60 cm (Z), and is covered

9.4 Case 4: Heat Balance of the Spacecraft Body - No Sun

in black-Kapton MLI. The +X face of the Payload Box has the Coronagraph aperture (15 cm diameter) and the -X face has the Coronagraph OSR radiator panel 20 cm \times 20 cm. It is worth noting that the interior panels and module boxes are left with their natural metallic surfaces (alochromed in the case of the avionics modules).

In the nominal sun pointing position, heat from the Sun falls on the +X body panel. This results in a solar heat panel of 75 W, which, combined with the internal power losses envisaged by Mode 1 (50 W, considering the 20 W dissipated in the separate Payload box), result in a total input power of 125 W. At equilibrium, the temperature of spacecraft box in the case of a five-layer MLI cover would be -11° C. This is too cold and thus it would require some design modifications to increase its temperature.

By removing the Optical Solar Reflector radiator panels, the temperature of the spacecraft bus is found to be 15° C in Mode 1. This value is found to increase up to 53.9° C when the spacecraft is not only in full sun light but also communicating data down to Earth (Mode 4, internal dissipation equal to 132 W). Both of these body temperatures are acceptable, which is why a decision to remove the OSR radiator panels is advocated. We highlight that, although acceptable, MLI blankets surrounding the propellant tanks can contribute to keeping the propellant temperature at the nominal desired value of 40° C.

9.4 Case 4: Heat Balance of the Spacecraft Body - No Sun

In eclipse, the spacecraft will be carrying out scientific observations, with and without heaters (power dissipation mode 2 and 3, respectively). In both of these modes, 40 W of power are dissipated separately in the payload box, resulting in a spacecraft body heat of 70 W and 239 W, respectively.

Due to eclipse conditions, the spacecraft receives zero solar heat power, which brings the temperature of the interior of the spacecraft down to -23.7° C. This is rather cold for the spacecraft interior, which is why the utilisation of spacecraft heaters is recommended. With the inclusion of spacecraft heaters, the temperature of the spacecraft body raises to a much higher level of 65.8° C. This higher temperature suggests that some spacecraft heaters may be turned off to save power or guarantee redundancy.

10. POWER BUDGET

A power budget assessment has been carried out to estimate the battery pack mass as well as the total

power consumed by the spacecraft in a fully operational mode (All payloads ON + Data downlink + Active thermal control + AOCS actuations, etc etc). regulators.

Item	Power [W]	Note
Payload Power	40	All instruments are ON
Min. Power Comms	20	Secondary Payloads are always ON
	40	Data downlink mode
	2	quiescent
TTC	2	
Rx	4	
OBC	4	10 W peak
SSDR	2	10 W peak
ADCS	4	
RWs	8	4x 2W
Prop. Cont.	2	
Thermal Cont.	2	
Power System	9.6	8 W + 20% of Avionics Stack Power
Prop. Heaters	20	bi-propellant, 10 W + 10 W
Solar Array Heater	120	Two panels, 60 W each
Battery Heater	10	Only during Total eclipses
Full Ops Peak	269.6	

Fig. 21: Power Budget Analysis for the MESOM spacecraft.

Using the worst case assumptions of Fig. 21, the power capacity of the MESOM battery pack can be calculated as the total peak power consumption (269 W) times the duration of the worst total eclipse (10 hr). The battery capacity is further increased to 3975 W hr in order to account for depth of discharge and discharge. Assuming state-of-the-art values for spacecraft battery capabilities (150 W hr/kg and 300 W hr/l, for mass and volume calculations, respectively), it is found that the battery pack of the MESOM spacecraft may have a mass and volume values of 26.5 kg and 13.25 l, respectively. These quantities are considered to be above “average”, but certainly within reach of currently available technologies. The $\simeq 14$ l volume of the battery pack can be also easily accommodated on the designated spacecraft bus without interference with the baselined payload design.

11. MASS BUDGET

Figure 22 summarizes the mass budget analysis for the MESOM spacecraft. The estimated dry mass and wet mass of the spacecraft are found to be 254 kg and 344 kg, respectively.

12. CONCLUSIONS & FUTURE STEPS

This paper summarized the preliminary trajectory design analysis and systems engineering trade-

Estimate Mass of Spacecraft Bus			Estimate Mass of Avionics Stack		
	Mass of Propulsion Bay Baseplate honeycomb	20		Comm box	2
	Mass of Payload Bay Baseplate	20		TTC box	2
	Mass of side/tie panels honeycomb	13		Rx box	2
	Mass of avionics panel honeycomb	12		OBC box	2
	Nuts/bolts/inserts/fixings	8		SSDR box	2
	add 10% margin	7.3		ADCS box	2
		80.3		Prop controller	2
	Attach Fitting	5		thermal controller	2
2	Mass of 4x Reaction Wheels	8	0.5	Mass of harness	4
	Estimate Mass of Propellant Tanks		4	2x Power Boxes	8
	Mass of Propellant Tank	11.5	1	2x Power Harness Boxes	2
	Heaters	0.5		Add 10% margin	3
	Add 10% margin	1.2			33
		13.2		Mass of Antenna (1 m diameter aluminium dish)	5
	Estimate Mass of Bi-propellant Engine			Mass of Solar Arrays	24
	Pipework	4		Mass of Battery Pack	26
0.65	4x 10 N MMH/MON thruster (delta-v delivery)	2.6			
0.29	6x 1 N MMH thruster (attitude)	1.74		Total Spacecraft Bus Mass	214
	Valves	1		Mass of Payload	40
	He pressure tank	8		Spacecraft Dry Mass	254
	add 10% margin	1.734			
		19.074		Propellant Mass	90
				Spacecraft Wet Mass	344 kg

Fig. 22: Mass Budget Analysis for the MESOM spacecraft.

offs of a Moon-Enabled Sun Occultation Mission (MESOM). A (2:1) synodic resonant, Earth-centred, retrograde orbit was found to deliver monthly and manoeuvre-free high-quality measurements of the inner sun corona while coping with the gravitational attraction of the Earth, Sun and Moon. A suite of scientific instruments was therefore proposed to capitalize on UK expertise in ground-based total eclipse observations while addressing key knowledge gaps that could contribute to revolutionize our understanding of the Sun and adverse space weather phenomena.

A payload of 40 kg and 40 W may be supported via a mini-satellite bus such as the SSTL's GMP, offering extensive flight heritage and flexibility. Indeed, the $1.3 \times 1.3 \times 1.4$ m platform, with its $0.8 \times 0.9 \times 0.6$ m payload box situated on top, can be carried by a wide range of launch vehicles, and has an all up wet mass of less than 400 kg. This is comfortably above the estimated wet mass of the MESOM spacecraft, which was pinned down to 344 kg after preliminary trade-off analyses and numerical simulations.

By making use of electrical heaters—particularly on the deployed, tracking solar panels—and also on critical items in the spacecraft body, such as the propellant tanks and battery pack, it has been possible to accommodate the wide range of thermal environments encountered throughout the baselined MESOM trajectory, and maintain subsystems within their safe operational range. These findings can be used to corroborate the feasibility of MESOM and to

establish a baseline for maturing this original concept into a successful spacecraft mission.

ACKNOWLEDGMENT

This research was funded by the UK Space Agency under the National Space Technology Programme. NB is thankful to Mr. Dikko Ladan-Baki for his contributions to the navigation analyses of MESOM.

REFERENCES

- [1] JP Eastwood, E Biffis, MA Hapgood, L Green, MM Bisi, RD Bentley, Robert Wicks, L-A McKinnell, M Gibbs, and C Burnett. The economic impact of space weather: Where do we stand? *Risk analysis*, 37(2):206–218, 2017.
- [2] Léonard Bolduc. Gic observations and studies in the hydro-québec power system. *Journal of Atmospheric and Solar-Terrestrial Physics*, 64(16):1793–1802, 2002.
- [3] Richard C Carrington. Description of a singular appearance seen in the sun on september 1, 1859. *Monthly Notices of the Royal Astronomical Society*, 20:13–15, 1859.
- [4] JS Halekas, GT Delory, DA Brain, RP Lin, MO Fillingim, CO Lee, RA Mewaldt, TJ Stubbs, WM Farrell, and MK Hudson. Extreme lunar

- surface charging during solar energetic particle events. *Geophysical research letters*, 34(2), 2007.
- [5] Masayuki Naito, Nobuyuki Hasebe, Mana Shikishima, Yoshiharu Amano, Junichi Haruyama, Jose A Matias-Lopes, Kyeong Ja Kim, and Satoshi Kodaira. Radiation dose and its protection in the moon from galactic cosmic rays and solar energetic particles: at the lunar surface and in a lava tube. *Journal of Radiological Protection*, 40(4):947, 2020.
 - [6] GE Brueckner, RA Howard, MJ Koomen, CM Korendyke, DJ Michels, JD Moses, DG Socker, KP Dere, PL Lamy, A Llebaria, et al. The large angle spectroscopic coronagraph (lasco) visible light coronal imaging and spectroscopy. *The SOHO mission*, pages 357–402, 1995.
 - [7] Robert M MacQueen, A Csoeke-Poeckh, E Hildner, L House, R Reynolds, A Stanger, H Tepoel, and W Wagner. The high altitude observatory coronagraph/polarimeter on the solar maximum mission. *Solar Physics*, 65(1):91–107, 1980.
 - [8] V Domingo, B Fleck, and Arthur I Poland. The SOHO mission: an overview. *Solar Physics*, 162(1):1–37, 1995.
 - [9] S Eckersley and S Kemble. A method of Solar Occultation. European Patent No. EP2641833B1.
 - [10] Nicolò Bernardini, Nicola Baresi, Roberto Armellin, Steve Eckersley, and Sarah A Matthews. Trajectory design of earth-enabled sun occultation missions. *Acta Astronautica*, 2022.
 - [11] S Rifai Habbal, H Morgan, M Druckmüller, A Ding, JF Cooper, A Daw, and EC Sittler. Probing the fundamental physics of the solar corona with lunar solar occultation observations. *Solar Physics*, 285:9–24, 2013.
 - [12] John F Cooper, Shadia R Habbal, Benjamin Boe, Vassilis Angelopoulos, David G Sibeck, Nikolaos Paschalidis, Edward C Sittler Jr, Lan K Jian, and Rosemary M Killen. Lunar solar occultation explorer (lunasox). *Frontiers in Astronomy and Space Sciences*, 10:1163517, 2023.
 - [13] Jaroslav Bartoněk, Václav Lazar, Petr Malaník, Štěpán Rydlo, Tomáš Lázníčka, Robert Popela, and Miloslav Druckmüller. Low earth orbit determination in small satellite mission proposal for corona observation of close solar surface region. *Acta Astronautica*, 203:202–213, 2023.
 - [14] Emily M Zimovan-Spreen, Kathleen C Howell, and Diane C Davis. Near rectilinear halo orbits and nearby higher-period dynamical structures: orbital stability and resonance properties. *Celestial Mechanics and Dynamical Astronomy*, 132(5):28, 2020.
 - [15] Kenza K Boudad, Kathleen C Howell, and Diane C Davis. Dynamics of synodic resonant near rectilinear halo orbits in the bicircular four-body problem. *Advances in Space Research*, 66(9):2194–2214, 2020.
 - [16] Takuya Chikazawa, Nicola Baresi, Stefano Campagnola, Naoya Ozaki, and Yasuhiro Kawakatsu. Minimizing eclipses via synodic resonant orbits with applications to equuleus and mmx. *Acta Astronautica*, 180:679–692, 2021.
 - [17] Daniel Villegas-Pinto, Nicola Baresi, Slim Lochocoche, and Daniel Hestroffer. Resonant quasi-periodic near-rectilinear halo orbits in the elliptic-circular earth-moon-sun problem. *Advances in Space Research*, 71(1):336–354, 2023.
 - [18] G. J. Gómez, J. Llibre, R. Martínez, and Masdemont. *Dynamics and Mission Design Near Libration Points*, volume II, chapter The Equations of the Bicircular Problem, pages 16–19. Wolrd Scientific Publishing, 2001.
 - [19] V Szebehely. Theory of orbits-the restricted problem of three bodies. *Soviet Astronomy*, 13:364, 1969.
 - [20] R. A. Broucke. Periodic orbits in the restricted three-body problem with earth-moon masses. Technical report, NASA, 1968.
 - [21] Ricardo L. Restrepo and Ryan P. Russell. A database of planar axisymmetric periodic orbits for the Solar system. *Celestial Mechanics and Dynamical Astronomy*, 130(7):49, July 2018.
 - [22] Rüdiger Seydel. *Practical bifurcation and stability analysis*, volume 5. Springer Science & Business Media, 2009.
 - [23] Stefano Campagnola, Naoya Ozaki, Yoshihide Sugimoto, Chit Hong Yam, Hongru Chen, Yosuke Kawabata, Satoshi Ogura, Bruno Sarli,

- Yasuhiro Kawakatsu, Ryu Funase, et al. Low-thrust trajectory design and operations of procyon, the first deep-space micro-spacecraft. In *25th International Symposium on Space Flight Dynamics*, volume 7. German Aerospace Center (DLR) Munich, Germany, 2015.
- [24] Philip E Gill, Walter Murray, and Michael A Saunders. Snoop: An sqp algorithm for large-scale constrained optimization. *SIAM review*, 47(1):99–131, 2005.
- [25] Arthur J Schwaniger. Trajectories in the earth-moon space with symmetrical free return properties. Technical report, National Aeronautics and Space Administration, 1963.
- [26] Mark Jesick and Cesar Ocampo. Optimal lunar orbit insertion from a variable symmetric free-return trajectory. *Journal of guidance, control, and dynamics*, 34(6):1867–1875, 2011.
- [27] Kenshiro Oguri, Kenta Oshima, Stefano Campagnola, Kota Kakihara, Naoya Ozaki, Nicola Baresi, Yasuhiro Kawakatsu, and Ryu Funase. Equuleus trajectory design. *Journal of the Astronautical Sciences*, 67(3):950–976, 2020.
- [28] Wang Sang Koon, Martin W Lo, Jerrold E Marsden, and Shane D Ross. *Dynamical systems, the three-body problem and space mission design*. World Scientific, 2000.
- [29] Bernhard Fleck. SOHO Factsheet. <https://sohowww.nascom.nasa.gov/about/about.html>, 2003. [Online; Accessed 06-03-2022].
- [30] GE Brueckner, RA Howard, MJ Koomen, CM Korendyke, DJ Michels, JD Moses, DG Socker, KP Dere, PL Lamy, A Llebaria, et al. The large angle spectroscopic coronagraph (lasco) visible light coronal imaging and spectroscopy. *The SOHO mission*, pages 357–402, 1995.
- [31] Samuel Tun. Description of the lasco instrument aboard soho. Technical report, Citeseer, 2005.
- [32] Pamela C Sullivan. Goes-r series spacecraft and instruments. In *The GOES-R Series*, pages 13–21. Elsevier, 2020.
- [33] Robertus Erdélyi, Luc Damé, Andrzej Fludra, Mihalís Mathioudakis, T Amari, B Belucz, F Berrilli, S Bogachev, D Bolsée, V Bothmer, et al. Hirise-high-resolution imaging and spectroscopy explorer-ultrahigh resolution, interferometric and external occulting coronagraphic science. *Experimental Astronomy*, 54(2):227–256, 2022.
- [34] Liam Edwards, Kaine A Bunting, Brad Ramsey, Matthew Gunn, Tomos Fearn, Thomas Knight, Gabriel Domingo Muro, and Huw Morgan. Derived electron densities from linear polarization observations of the visible-light corona during the 14 december 2020 total solar eclipse. *Solar Physics*, 298(12):140, 2023.
- [35] Gabriel D Muro, Matt Gunn, Stephen Fearn, Tomos Fearn, and Huw Morgan. Visible emission line spectroscopy of the solar corona during the 2019 total solar eclipse. *Solar Physics*, 298(6):75, 2023.
- [36] Liam Edwards, Kaine A Bunting, Brad Ramsey, Matthew Gunn, Tomos Fearn, Thomas Knight, Gabriel Domingo Muro, and Huw Morgan. Derived electron densities from linear polarization observations of the visible-light corona during the 14 december 2020 total solar eclipse. *Solar Physics*, 298(12):140, 2023.
- [37] Benjamin Boe, Shadia Habbal, Miloslav Druckmüller, Adalbert Ding, Jana Hodérova, and Pavel Štarha. Cme-induced thermodynamic changes in the corona as inferred from fe xi and fe xiv emission observations during the 2017 august 21 total solar eclipse. *The Astrophysical Journal*, 888(2):100, 2020.
- [38] Adalbert Ding and Shadia Rifai Habbal. First detection of prominence material embedded within a 2×10^6 km cme front streaming away at 100–1500 km s⁻¹ in the solar corona. *The Astrophysical Journal Letters*, 842(1):L7, 2017.
- [39] F. Lei and et al. Development of compact cerenkov proton detectors and telescopes. In *UKSWSE Conference, Exeter*, 2024.
- [40] John Liddle, Lucy Edge, Wies Tondryk, David Peilow, and A Garutti. Giove-a and gmp: Sstl’s meo and geo satellite family-first in-orbit test results. In *24th AIAA International Communications Satellite Systems Conference*, page 5329, 2006.
- [41] James Richard Wertz, Wiley J Larson, Douglas Kirkpatrick, and Donna Klungle. *Space mission analysis and design*, volume 8. Springer, 1999.

- [42] W. A. Imbriale. Computing the Noise Temperature Increase Caused by Pointing DSS 13 at the Center of the Moon. *Interplanetary Network Progress Report*, 42-166:1–10, August 2006.
- [43] Roger Walker, D Koschny, C Bramanti, I Carnelli, ECS Team, et al. Miniaturised asteroid remote geophysical observer (m-argo): a stand-alone deep space cubesat system for low-cost science and exploration missions. In *6th Interplanetary CubeSat Workshop, Cambridge, UK*, volume 30, 2017.
- [44] CP Bridges. Star-xl: student transponder for satellite ranging on x & l-band. In *4th Symposium on Space Educational Activities*. Universitat Politècnica de Catalunya, 2022.
- [45] M Necati Özişik, Helcio RB Orlande, Marcelo Jose Colaco, and Renato Machado Cotta. *Finite difference methods in heat transfer*. CRC press, 2017.